Analysis of a textural atomization process

Christophe Dumouchel, Jean-Bernard Blaisot, Fakhry Abuzahra, Akira Sou, Gilles Godard, Saïd Idlahcen

Analysis of a textural atomization process

Christophe Dumouchel[1*], Jean-Bernard Blaisot[1], Fakhry Abuzahra[1], Akira Sou[2], Gilles Godard[1], Said Idlahcen[1]

1: CORIA – UMR 6614, Normandie Université, Université et INSA de Rouen, Saint-Etienne du Rouvray, France

2: Department of Mechanical Engineering, Kobe University, Kobe, Japan

*: Corresponding author: Christophe.dumouchel@coria.fr

Abstract

The experimental work reported in this paper addresses the question of the description of a textural atomization process including the atomizing structures and the resulting drops. Textural atomization process designates a deformation leading to drop-production localized on the liquid-gas interface of a liquid flow: droplets appear like peeled from the interface. Such a process usually takes place in the near field region, i.e., near the injector. In the present work, the textural atomization process of a cavitating liquid flow is considered. A multiscale method is applied to describe this process and the concept of equivalent-system of cylinders is introduced and sued to provide a mathematical expression for it. In parallel, a mathematical formulation for the measured drop diameter-distribution is presented also. The connection between the atomization process and the spray is established on the basis of these mathematical formulations. It brings a model in which the main-drop diameter-distribution is controlled by the size distribution of the ligaments of the textural atomization process, and the satellite-drop peak links with their deformation. This analysis demonstrates that the scales for which the successive derivatives of the scale distribution are zero are characteristic lengths of the spray drop diameter distributions. These results have a potential to elaborate new simulation strategies for instance.

Acknowledgments

This project has received funding from the European Union Horizon-2020 Research and Innovation Programme. Grant Agreement No 675676

1. Introduction

The most frequent method to produce a spray is to eject a liquid flow in a gaseous medium thanks to a device called an atomizer or an injector. Several concepts of injector and atomizer exist (Lefebvre, 1986). As soon as the liquid flow emerges from the atomizer, perturbations deform it and some of them grow in such proportion that liquid fragments detach from the bulk flow. This process is referred in the literature as the primary atomization process. The fragments issued from the primary process may deform to their turn and breakup into smaller fragments, and this, until the cohesive surface tension forces are strong enough to oppose extra fragmentation. This second step is called the secondary atomization process. The resulting flow of drops of different size and velocity is the spray.

The primary atomization process can be subdivided into two drop production processes. Some liquid fragments and droplets may be peeled from the liquid gas interface while others result from the breakup of the liquid bulk. The first source depends on the *local* kinematic and geometrical characteristics of the liquid-gas interface whereas the second one depends on the *global* kinematic and geometrical characteristics of the liquid bulk. These two drop production mechanisms will be referred here as *textural* and *structural* atomization process, respectively. This designation is inspired by Kaye (1989) who introduced the textural and structural fractal dimension to differentiate the local boundary tortuosity of a system from its global shape or deformation. The textural atomization process is a near field mechanism, i.e., it is usually triggered soon after the liquid issues from the atomizer.

The Rayleigh-Taylor instability developing on an air-assisted laminar jet (Marmottant and Villermaux, 2004) and that produces streamwise ligaments, which eventually break up into droplets, can be seen as a textural atomization process. However, in most cases, textural atomization processes are imposed by the issuing flow characteristics. They manifest by an increase of tortuosity of the issuing-flow interfaces. The textural fractal dimension characterizing this tortuosity has been found to correlate with the issuing flow Reynolds number (Grout et al. 2007). This tortuosity is usually due to the emergence of rather ligamentary structures whose sizes are far smaller than the one of the bulk flow. A nice example of this was reported on laminar jets for which the vorticity distribution in the liquid near the interface, triggers the development of small ligaments from which droplets emanate (Wu et al. 1995). The development and disintegration of these ligaments are fast mechanisms and result in the production of a spray around the liquid jet with the effect of increasing the flow angle at the nozzle exit. In some conditions, this spray can be rather dense. This is the case in applications that combine high injection pressures and small orifice dimensions, as, for instance, in car fuel injection. In such situations, it is important to account for the textural atomization mechanism in the design of the injection process. However, textural atomization has been barely investigated so far.

The present investigation aims of providing experimental measurements and mathematical descriptions of a textural atomization process and of the drop size-distribution of the spray resulting from this process. Establishing the correlation between the structures involved in the textural atomization process and the drop sizes is an objective of the work also. The situation examined concerns cavitating injection conditions.

Cavitation is an important mechanism in liquid injection, and part of its influence could be precisely related to the textural atomization. It designates a phase change of the liquid in the injector due to an excessive stress (Dumont et al. 2000). This results in the production of gaseous bubbles and structures in the flow that may or not reach the nozzle exit and that modify the characteristics of the flow issuing from the nozzle. Flows with a sudden section reduction are prompt to cavitate. Detachment of the boundary layer at the entrance of the downstream canal may occur and favor the development of a recirculation zone that actually squeezes the main flow passage. This is the *vena contracta* mechanism. The pressure at the vena contracta decreases when the flow rate is increased, and the liquid phase change occurs when this pressure has become lower than the liquid vapor pressure. Many experimental works of the literature have reported four flow regimes in

cylindrical injector orifices when the flow rate is increased, i.e., Regime I: no-cavitation; Regime II: developing cavitation; Regime III: super-cavitation; and Regime IV: hydraulic flip. Regime I concerns the low flow rates for which no cavitation is observed.
The appearance of cavitation bubbles at the entrance of the orifice marks the beginning of the developing cavitation regime (Regime II). Being caused by the injector geometry, these cavitation structures are said geometrically induced. In the super-cavitation regime (Regime III), the geometrically induced cavitation structure increases in length and may extend to the nozzle exit section. The length of the cavitation structure varies because of cavitation shedding which designates the expulsion of bubble clouds that may either collapse before reaching the nozzle exit or reach the nozzle exit before collapsing. Numerous experimental observations (Arai et al. 1985, Sou et al. 2008, among others) reported an increase of the flow angle at the nozzle exit in this regime, which reveals the presence of a textural atomization process. The hydraulic flip regime (Regime IV) occurs when the cavitation vanishes because external air moves upstream between the flow and the orifice wall. The characteristic feature of this regime is to produce smooth and unperturbed liquid jets. The flow regime characteristics are very much influenced by the internal design of the injector, and, in particular, to sharp direction changes (Sou 2012). Detailed in Section 3, the atomizer selected for this experimental work presents such a characteristic.

The present work must address the crucial question of atomization process and spray description. The number of experimental studies treating the question of the atomization process remains rather low. The temporal evolutions of the liquid-gas interface area and of its shape are appropriate quantities to describe the process. The knowledge of the interface shape is important since it informs on the interface deformation or tortuosity that structures the atomization process. The fractal dimension concept may characterize this tortuosity but cannot provide a full description of the atomization process because it involves a scale range wider than the one for which self-similarity is observed (Shavit and Chigier 1995, Grout et al. 2007). This result motivated the development of a multiscale method that introduces the scale distribution to describe any system whatever its shape (Dumouchel 2017). As reported in several applications, (Dumouchel et al. 2015a, Dumouchel et al. 2015b, Tirel et al. 2017, Vu and Dumouchel 2018) it may give access to the dynamics of the interface deformation as a function of the scale, i.e., as a function of the structure size and shape involved in the atomization process.
The multiscale method will be applied here to measure the average scale distribution of the interfaces at the nozzle exit. An analysis, aiming to establish a mathematical formulation for this distribution, will be then performed. It is based on the concept of equivalent systems which designates systems having the same scale distribution although their shapes are different. Using this concept, the scale distributions of ensemble of non-spherical drops received a mathematical formulation built from the diameter distribution of the equivalent system of spheres (Dumouchel et al. 2015a). For the first time, this concept will be applied by considering equivalent systems of cylinders. It will be shown that, in 2D, which is the embedded dimension imposed by any image analysis approach, any system has an equivalent system of cylinders. A mathematical formulation for the atomization process scale distribution could be therefore established from the diameter

distribution of the equivalent system. This approach is very appealing in the present context where the textural tortuosity is expected to result from the presence of ligaments whose 2D projections resemble cylinders. Therefore, establishing a mathematical scale distribution addresses the question of the mathematical representation of size distribution, question that concerns the spray drop size also.

The question of a universal mathematical expression for the drop diameter-distribution of liquid spray has been largely debated in the community (Lefebvre 1986, Babinsky and Sojka 2002, Villermaux 2007, Dumouchel 2009) but it remains unanswered. One of the main reasons could be that none of the approaches is based on a fine description of the atomization process. In the context of this work, diameter distributions will be represented by a 3 parameter Generalized-Gamma (3pGG) function. It has modeling foundations and covers a wide range of mathematical and empirical distributions of the literature (Dumouchel 2006). Furthermore, the good ability of this function to fit experimental drop diameter-distributions has been reported in many different situations (Lecompte and Dumouchel 2008, Fdida et al. 2018). The 3pGG function is going to be applied twice: 1 – for the textural atomization process analysis to represent the diameter distribution of the cylinder equivalent system, 2 – for the spray analysis to represent the drop diameter distribution.
Section 2 presents the mathematical elements concerning the 3pGG function and the multiscale method. The experimental work is detailed in Section 3 and the last section is dedicated to the analysis of the experimental results. The article ends with a short conclusion.

2. Mathematical elements

The spray drop-diameter distribution

From a mathematical point of view, the drops are considered spherical (each of them is fully defined with one diameter D) and the diameter-distribution characterizes the spray system. The determination of a mathematical function to represent spray drop-diameter distribution remains an open scientific issue. The methods used to this aim were reviewed by Babinsky and Sojka (2002). The mathematical spray drop diameter-distribution used in this work is the 3pGG function which expresses as (Dumouchel 2006):

$$f_n(D) = \frac{q}{\Gamma\left(\frac{\alpha+n}{q}\right)}\left(\frac{\alpha}{q}\right)^{\frac{\alpha+n}{q}} \frac{D^{\alpha+n-1}}{D_{q0}^{\alpha+n}} exp\left(-\frac{\alpha}{q}\left(\frac{D}{D_{q0}}\right)^q\right) \qquad n = 0, 1, 2, 3 \qquad (1)$$

where Γ is the Gamma function and D_{q0} is the q^{th} order mean diameter of the mean-diameter series introduced by Mugele and Evans (1951). The parameter n allows distinguishing the distribution type: $f_0(D)$ is the number-based diameter distribution, $f_1(D)$ the length-based diameter distribution, $f_2(D)$ the surface-based diameter distribution, and $f_3(D)$ the volume-based diameter distribution. The dimension of the distributions is the inverse of a length, and every distribution is normalized.

The 3pGG function depends on the three parameters q, α and D_{q0}. D_{q0} has the dimension of a diameter and q and α have no dimension. These two parameters can be positive or negative, but they must have the same sign (Dumouchel 2006). In this work, they will be taken positive. The distributions for $n > 0$ are mono-modal, i.e., they have a bell shape and exhibit a single maximum called the peak diameter D_{pn}. The number-based diameter distribution reports the same characteristic provided that $\alpha > 1$.

The preference for selecting the 3pGG function among the numerous proposals found in the literature is based on the following facts. First, this function covers many mathematical distributions of the literature such as the Weibull, the Rosin-Rammler, the Nukiyama-Tanasawa distributions (Dumouchel 2006). Second, the 3pGG functions allows performing calculations. For instance, the mean-diameter series of Mugele and Evans (1951) writes:

$$D_{kl}^{k-l} = \left(\frac{q}{\alpha}\right)^{\frac{k-l}{q}} \frac{\Gamma\left(\frac{\alpha+k}{q}\right)}{\Gamma\left(\frac{\alpha+l}{q}\right)} D_{q0}^{k-l} \tag{2}$$

where k and l can take any real values provided that $k \neq l$. The peak diameter D_{pn} of the distribution appears to be a specific mean diameter of this series and writes:

$$D_{pn} = D_{q+n-1,n-1} \qquad n = 0, 1, 2, 3 \tag{3}$$

Third, in the context of liquid atomization, the 3pGG function has received theoretical foundations twice. First, the atomization model, based on the agglomeration mechanism of unit elements that compose the liquid system (Villermaux et al., 2004), has led to a mathematical expression for the spray drop-diameter distribution that corresponds to a 3pGG function with $q = 1$. Second, the 3pGG function has been found to be the solution of a model based on the Maximum Entropy Formalism (Dumouchel 2006, 2009). In this model, the three parameters have been introduced to ensure the bell shape of the distribution: the parameter q mainly controls the distribution in the large-diameter range, and the parameter α controls the distribution in the small-diameter range. The third parameter positions the distribution in the diameter space. An example of 3pGG number-based distributions with several values of α is shown in Fig. 1. This figure indicates that a decrease of α spreads the distribution in the small diameter range: the dispersion of the distribution in the small-diameter range increases. A similar dependence is found between the parameter q and the dispersion of the distribution in the large-diameter range.

The atomization process scale distribution

The multiscale method used to describe the atomization process has been applied in many situations including atomizing turbulent liquid sheets, car injector fuel jet, capillary jet instability (Dumouchel, 2017) and viscoelastic capillary jet instability (Tirel et al., 2017). This is an image

analysis method that measures the scale distribution of a system whatever its shape. This measurement is performed on segmented images (two gray level images) where the liquid appears in black on a white background. Inspired from the Euclidean Distance Mapping method to measure fractal dimension (Bérubé and Jébrak 1999), the cumulative scale distribution $E_2(d)$ is first measured from successive erosion operations with a circular structural element of diameter d ranging from 0 to infinity (Soille 2004). The diameter d is named the scale in the following. $E_2(d)$ is the relative amount of surface area removed by the erosion operation at scale d (Dumouchel et al. 2008, Dumouchel 2017). Second, the scale distribution $e_2(d)$, defined as the derivative of the cumulative scale distribution in the scale space, is calculated:

$$e_2(d) = \frac{\mathrm{d}E_2(d)}{\mathrm{d}d} = \frac{P(d)}{2S_T} \tag{4}$$

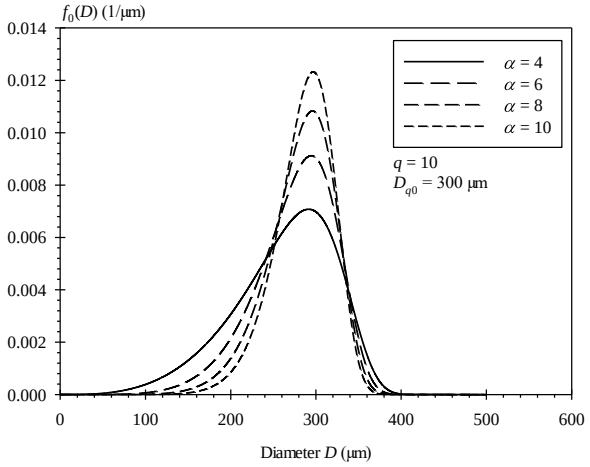

Fig. 1 Example of 3pGG number-based diameter distribution for several values of the parameter α (q = 10; D_{q0} = 300 μm)

As mentioned in Eq. (4), the scale distribution $e_2(d)$ is equal to the ratio of the perimeter $P(d)$ of the system eroded at scale d on twice the total surface area S_T of the system. As for the spray diameter distribution, the scale distribution is normalized and its dimension is the inverse of a length. Furthermore, by construction and since the perimeter $P(d)$ can only decrease as d increases, the scale distribution is always maximum for $d = 0$. Finally, $e_2(d)$ is a derivable function.

Examples of the scale distributions for three systems are plotted in Fig. 2. Image 1 is the one of a cylinder. Using image analyzing tools available in the ImageJ software, the cumulative scale distribution was measured on this image and derived to get the scale distribution $e_2(d)$. As shown in the figure, the scale distribution of such a deformation-free system is a step function. Image 2 is the one of a system with textural structures. The corresponding scale distribution displays a high value of $e_2(0)$ illustrating the increase of the system perimeter brought by the textural structures. Then, as the scale increases, the scale distribution decreases in proportion with the contour length that decreases since textural structures disappear by order of size during the successive erosion operations. For higher scales, the central portion of the system, identical to image 1, remains only and the scale distribution adopts a step-like behavior. Image 3 is the one of a system with a body deformation. The corresponding scale distribution remains flat for the small scales for which the structural deformation is not perceptible, but decreases in the large-scale range

in proportion to the erosion operations that, step by step, erase all structures by order of size. In this case, the interface perimeter depends mainly on large characteristic length deformation.

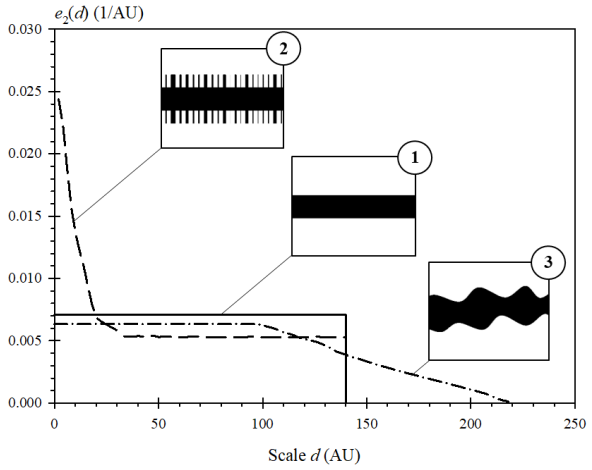

Fig. 2 Examples of scale distribution $e_2(d)$ (Case 1: No deformation; Case 2: Textural deformation; Case 3: Structural deformation)

It is also ambitioned in this work to give a mathematical expression for the scale distribution describing the textural atomization process. This will be achieved by using the concept of equivalent systems evoked in the introduction and, more precisely, by introducing the equivalent system of cylinders.

The cylinders considered here are defined with a diameter D and a height equal to unity. Furthermore, their analysis considers their lateral surface as interface only: the two circular section ends are not accounted. This vision of the cylinder is given by a portion of a cylindrical liquid fragment. The diameter distributions of such systems link with each other in a way different from systems of spheres due to the fact that the surface area of a cylinder is proportional to its diameter and not to the square of it as for spheres. The diameter-distributions $f_{nc}(D)$ of an ensemble of cylinders correlate as:

$$f_{nc}(D) = \left(\frac{D}{D_{n-1,0}} \right)^{n-1} f_{0c}(D) \qquad n = 2, 3 \tag{5}$$

Following the mathematical development conducted for ensembles of spheres (Dumouchel et al. 2008), it is possible to express the scale distribution of a cylinder ensemble as a function of its number-based diameter distribution. It comes:

$$e_2(d) = \frac{1}{D_{10}} \left(1 - \int_0^d f_{0c}(D)\, dD \right) \tag{6}$$

This equation can be used to determine the cylinder equivalent-system diameter distribution $f_{0c}(D)$ from the scale distribution $e_2(d)$ of the actual system. It comes:

$$f_{0c}(D) = -D_{10} \left[\frac{de_2(d)}{dd} \right]_{d=D} \tag{7}$$

Since the scale distribution is always derivable, Eq. (7) says that $f_{0c}(D)$ can always be determined. In 2D, any system accepts an equivalent system of cylinders. The number-based diameter distribution of this system is given by Eq. (7). We can consider for instance the case of a sphere of diameter D_s. The surface-based scale distribution of is this system defined in the range [0; D_s] only and is given by (Dumouchel et al. 2008):

$$e_2(d) = \frac{2}{D_s}\left(1 - \frac{d}{D_s}\right) \tag{8}$$

Introducing Eq. (8) in Eq. (7) returns $f_{0c}(D) = 1/D_s$ and $D_{10} = D_s/2$. Therefore, the ensemble of cylinders whose diameters are equiprobably distributed is equivalent to a sphere.
Equation (7) allows also establishing a mathematical formulation for $e_2(d)$ if $f_{0c}(D)$ has one. In particular, if $f_{0c}(D)$ is represented by a 3pGG function (Eq. (1)), the scale distribution writes:

$$e_2(d) = \frac{1}{D_{q0}}\left(\frac{\alpha}{q}\right)^{\frac{1}{q}} \frac{\Gamma\left(\frac{\alpha}{q}, \frac{\alpha}{q}\left(\frac{d}{D_{q0}}\right)^q\right)}{\Gamma\left(\frac{\alpha+1}{q}\right)} \tag{9}$$

where $\Gamma(a,b)$ is the upper incomplete Gamma function. In virtue of Eq. (7) and since the 3pGG function exhibits a single mode, Eq. (9) can represent scale distribution with a single inflexion point only. As for sphere ensembles, the parameters α and q control the dispersion of the distribution in the small and large-diameter ranges, respectively. When applied to a set of deformed ligaments, the scale distribution $e_2(d)$ in the large-scale region contains information on the ligament size distribution, whereas, in the small-scale range, it contains information on the ligament deformation. Therefore, when applying Eq. (9) to a set of deformed ligaments, the parameter q is sensitive to the ligament size distribution and the parameter α to the distribution of scales associated with their deformation. To our knowledge, this is the first time an atomization process receives a mathematical expression based on these concepts.

3. Experimental Setup and Results

Experimental setup and optical diagnostic

The atomizer used in the present work was designed and realized by Akira Sou. Its geometry is inspired from the internal path in Valve Covered Orifice nozzle that the fuel has to follow between the injector body and needle (Sou et al. 2012). One of the dominant features of this internal flow is the asymmetric entrance in the discharge orifice. This feature is reproduced in the atomizer made for this investigation and shown in Fig. 3. The liquid section is rectangular with a width of 4 mm

and a depth of 1 mm. The length of the discharge orifice is equal to 16 mm. The atomizer body is made of acrylic allowing observing the internal flow which is helped by the fact that all optical diopters are planar. The experimental setup is presented in Fig. 4. The liquid used is water (density ρ_L = 1000 kg/m^3, dynamic viscosity μ = 0.001 Pa.s, surface tension with air σ = 0.07 N/m, saturation vapor pressure P_v = 2339 Pa at 20°C). It is softened with a lime removal device and then kept in an open reservoir. A centrifugal pump (Perollo PQM 2900 rev/min) capable of providing a volume flowrate of 0.6 m^3/h at a pressure head of 7 bar, sucks the water and feeds the two loops of the circuit. One of the loops is a bypass that sends the water back to the reservoir. This loop contains a regulating valve and a 50 µm filter. The second loop feeds the atomizer. It is equipped with a flow meter, an on/off valve, a particle feeder system, a regulating valve, a thermocouple and a pressure gauge for the measurement of the reference injection pressure ΔP_i just before the atomizer entrance. The choice of this two loops configuration was motivated by the fact that the pump is unable to provide stable low flowrates. The total mass flowrate Q_{Tot} delivered by the pump is divided in two parts thanks to the use of the regulating valve positioned on the bypass loop. The effective mass flowrate Q_m is equal to (Q_{Tot} - Q_{Reg}), where Q_{Reg} is the mass flow rate in the bypass loop (see Fig. 4). The regulating valve in the second loop is used to accurately adjust low flowrates. The particle feeder system allows seeding the liquid flow with small particles in order to perform measurements of the flow velocity in the atomizers with a Laser Doppler Velocimetry system. All experiments are conducted at atmospheric pressure and temperature.

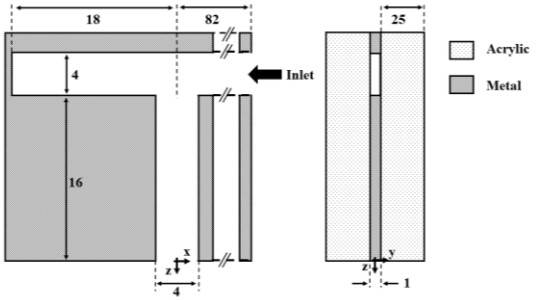

Fig. 3 Geometry of the atomizer (Left: front view, Right: side view, dimensions in mm, inlet arrow indicates flow entrance)

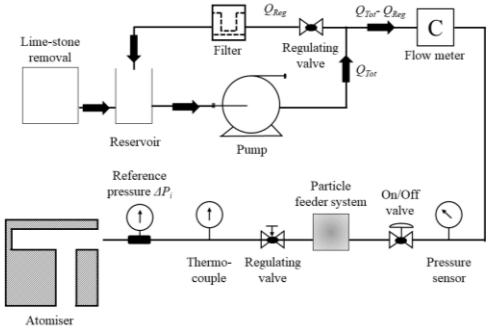

Fig. 4 Experimental setup

The mass flowrate Q_m is the parameter of the study. It was varied according to the values given in Table 1 where the corresponding reference injection pressures ΔP_i are also listed. The discharge coefficient C_D, defined as $Q_m/S_{or}(2\rho_L\Delta P_i)^{0.5}$ where S_{or} is the atomizer exit section, is calculated and appears rather constant (Table 1). This tells us that the axial flow carries the same proportion of the total initial energy for all cases. The flow average velocity V_q defined as $Q_m/(\rho_L S_{or})$ ranges from 10 m/s to 18.1 m/s. This velocity together with the thickness of the internal atomizer flow

(t_a = 1 mm, see Fig. 3) allows calculating the Reynolds number *Re* (= $\rho_L V_q t_a/\mu$) and the aerodynamic Weber number We_G (= $\rho_G V_q^2 t_a/\sigma$ where ρ_G is the air density). The Reynolds ranges from 10.10^3 and 20.10^3 which is representative of a sufficiently developed turbulence to trigger early perturbations on the issuing liquid flow interfaces. The aerodynamic Weber number remains low enough (less than 6) to consider that the aerodynamic forces have a negligible effect on the atomization process. The cavitation number *CN* is an indicator of the propensity of the internal flow to cavitate. The literature reports many formulations for this number. It generally compares the available amount of pressure to the pressure to be overcome to produce cavitation. The cavitation number chosen in this work is the one formulated by He and Ruiz (1995): $CN = (P_{amb} - P_v)/(0.5\rho_L V_q^2)$. This number accounts for the liquid vapor pressure in the expression of the pressure to be overcome to produce cavitation, and for the atomizer pressure-drop in the expression of the available pressure. A decrease of this number indicates an increasing propensity to cavitate. In the present work, *CN* ranges from 0.6 to 2 (Table 1), the lowest values being obtained for the highest flowrates.

Cond. N°	Q_m **(10^{-3}kg/s)**	ΔP_i **(bar)**	**Regime**	C_D **(-)**	V_q **(m/s)**	*Re* **(-)**	We_G **(-)**	*CN* **(-)**
1	40.0	2.7	I	0.43	10.0	10000	1.7	1.98
2	43.3	3.2	II	0.43	10.8	10800	2.0	1.69
3	47.5	3.9	II	0.43	11.9	11900	2.4	1.40
4	55.0	4.8	III	0.44	13.7	13700	3.3	1.05
5	57.5	5.3	III	0.44	14.4	14400	3.6	0.96
6	62.5	6.4	IV	0.44	15.6	15600	4.2	0.81
7	72.5	9.1	IV	0.42	18.1	18100	5.7	0.62

Table 1 Operating Conditions (Q_m: mass flow rate, ΔP_i: injection pressure, C_D: discharge coefficient, V_q: mean velocity, *Re*: Reynolds number, We_G: aerodynamic Weber number, *CN* is the cavitation number)

Internal and external flows are visualized in a diffuse back-light illumination configuration. The light source is a Quantel Ultra frequency doubled Q-Switched Nd:YAG laser (532 nm) whose pulse duration is equal to 6 ns, and the camera is a CCD Dalsa Pantera 11M4 (2672x4016 pixels). A Nikkon objective (300 mm f/4D) coupled with an extension tube allowed covering a physical field of 21.4 x 14.2 mm^2, which corresponds to a spatial resolution equal to 5.26 µm/pixel. (The maximum displacement during the light pulse is far less than 5.26 µm and all liquid structures are correctly frozen.) The images are temporally uncorrelated.

Image series have been taken to visualize the internal flow in the atomizer orifice, the atomization process at the nozzle exit, and the sprays. The internal flow and the atomization process are visualized on the front view ((0; x; z) plane, see Fig. 3). The atomization process images cover the region extending from the nozzle exit to 21.4 mm downstream. The spray drops are visualized on

the side view ((0; y; z) plane, see Fig. 3) since more drops are visible in this direction. These images covered the region extending from 40 mm to 54 mm. Each series counts 500 images.
All experiments were conducted with a rather constant liquid temperature of the order of 20°C.

Description of the internal and external flows

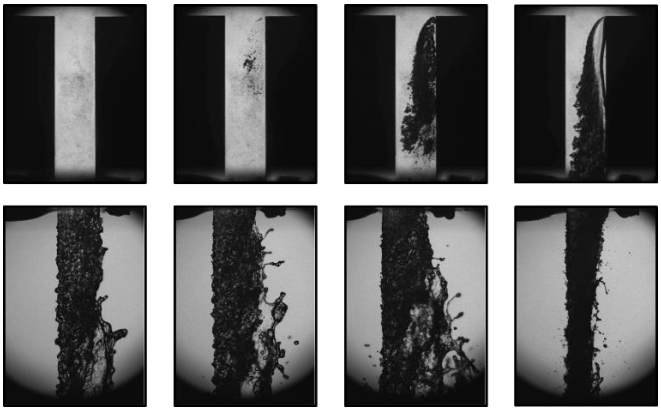

Fig. 5 Internal (top) and external (bottom) flow visualizations (from left to right: Cond 1-3-5-7)

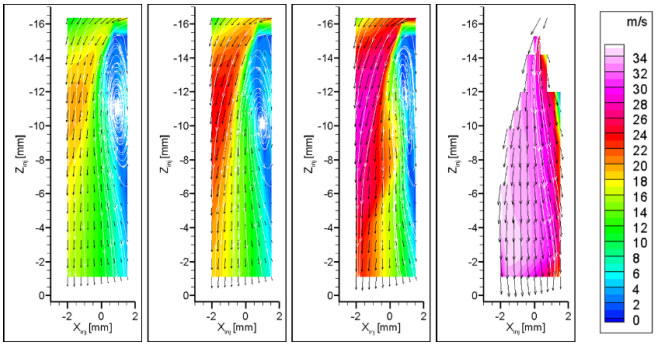

Fig. 6 Internal velocity field in the discharge orifice central plane (from left to right: Cond 1-3-5-7, LDV measurements)

Figure 5 shows internal and external-flow image-couples for four operating conditions. The top row presents the flow inside the atomizer orifice. The upper-channel flow comes from the right. The dark region that appears and develops as the flowrate increases is due to the presence of optical diopters that deviate the light. These diopters come from the presence of vapor resulting from cavitation in the liquid flow. The cavitation-structures are geometrically induced and they align with the boundary-layer detachment-wake. As expected, the dissymmetry of the atomizer induces a dissymmetry of the flow characteristics and its ability to cavitate. As reported by several experimental observations, the cavitation develops on the upstream side (right side in the image). The four images selected in Fig. 5 illustrate the four flow regimes identified in the atomizer orifice. From left to right, these regimes correspond to those reported in the literature (see Introduction), i.e., Regime I: no cavitation; Regime II: developing cavitation; Regime III: super cavitation; Regime IV: hydraulic flip. Because of the dissymmetry of the device, the hydraulic flip regime is of the "partial" type (Soteriou et al. 1995). These observations agree with those reported by Sou et al. (2012). The regimes corresponding to the present working conditions are given in Table 1. We confirm that a lower cavitation number *CN* is associated with an enhanced cavitation mechanism and note that flow Regime III corresponds to *CN* of the order of 1.

To complete the description of the internal flow, Fig. 6 presents the velocity of the flow in the middle plane of the orifice for the same four conditions as in Fig. 5. (These measurements were performed with the Laser Doppler Velocimetry technique.) For the three first regimes, a recirculation zone is visible in the discharge orifice along the upstream-side wall. First located at

the discharge orifice entry, this recirculation reinforces when the flow rate increases and disappears in the hydraulic flip regime where the flow slides along the wall with a rather high velocity. At the nozzle exit, the velocity profiles are always strongly dissymmetric which might enhance dissymmetric deformations of the issuing liquid flow.

The bottom row images in Fig. 5 show the atomization process associated with the four internal flow regimes. As expected, the dissymmetry of the liquid flow deformation is visible. The left interface presents a rather similar morphology for all cases: presence of small amplitude and small wavelength perturbations. The right interface (upstream-side interface) is more deformed and clearly exhibits a textural deformation involving the development of ligament structures and the production of drops. In Regime I, the ligaments are coarse but they get thinner and thinner and more and more numerous as the flowrate increases. We note also that Regimes I to III reveal a widening of the right side of the flow, behavior that has totally disappeared in Regime IV. This indicates a change of orientation of the flow resulting from the partial hydraulic flip of the internal flow. However, even for this regime, the ligament structures of the textural atomization process are well visible in this direction of visualization.

Atomization process scale distribution measurements and results

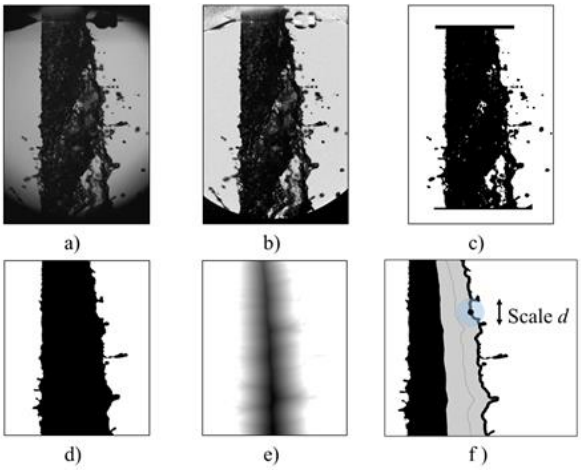

Fig. 7 Image analysis steps: a) raw image, b) normalized image, c) segmented image, d) holes filled and detached elements erased, e) EDM image, f) removed left part (black area) and erosion operation of the right part (gray area) of the flow

The images of the liquid flow issuing from the atomizer are analyzed in order to measure the scale distribution of the textural atomization process. As observed in Fig. 5, the textural atomization process is localized on the upstream-size interface and the measurement must account for this interface only. This is achieved by dividing the flow in two parts before performing the measurement. The main image treatment and measurement steps are summarized in Fig. 7. Each raw image (Fig. 7-a) is normalized (Fig. 7-b) and segmented (Fig. 7-c). In the segmented image (Fig. 7-c), the liquid appears in black on white background. These image treatment steps are performed with homemade routines (Fdida and Blaisot 2009). The holes in the liquid system are filled and the detached liquid elements are erased. They return the binary image (Fig. 7-d) on which the measurement sequence starts with the application of the Euclidean Distance Mapping. These operations are performed with the code ImageJ V. 1.50i and returns the image shown in Fig. 7-e. In this image, the lines made of the darker pixels constitute the skeleton of the object (Soille 2004). The vertical line of this skeleton is used to divide the system in two parts: the black and gray regions shown in Fig. 7-f. Finally, the erosion operations

at successive scales *d* is performed on the gray region only as illustrated in Fig. 7-f: at each value of *d*, the surface area lost by erosion is measured and the cumulative scale distribution is obtained. The smallest possible scale increment in the successive erosion operations is one pixel. In the present measurement, we selected a scale increment step of 7 pixels in order to reduce the number of data and to avoid surface variations too small to be correctly measured between two consecutive scales. The scale step of 7 pixels corresponds to 37 µm. The measurement of the cumulative scale distribution is performed on each image and derived to obtain the scale distribution. An area-weighted average scale distribution, $e_2(d)$: it represents the scale distribution of all textural structures that have been seen on the 500 proceeded images. It has been first checked that this number of images for far sufficient to get converged scale distributions.

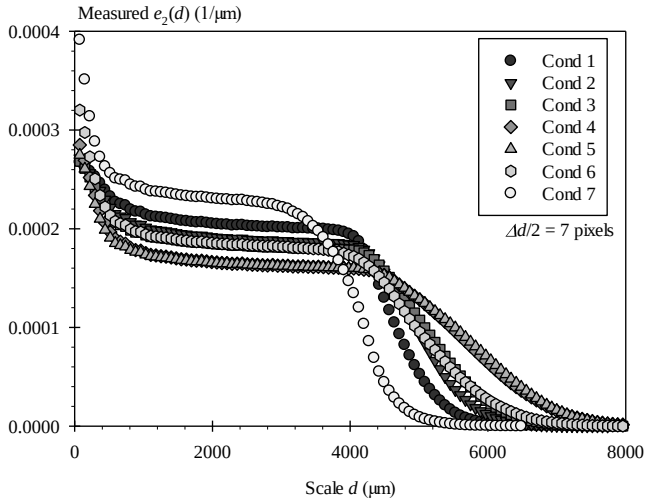

Fig. 8 Experimental scale distributions of the right part of the flow

The resulting scale distributions are plotted in Fig. 8. As the scale increases and for every case, the scale distribution first decreases sharply, second reaches a plateau, and third, follows another decrease to reach the value zero at a specific scale d_{max} called the maximum scale. Referring to Fig. 2, we understand that the decrease in the small-scale range is the signature of the textural atomization (case 2 in Fig. 2) that we precisely want to investigate. The decrease in the large-scale range characterizes the structural deformation of the half-flow (case 3 in Fig. 2). The plateau found in the middle-scale range indicates that no deformation is perceptible at these scales for which, therefore, the systems report a smooth-cylinder like behavior (case 1 in Fig. 2). As far as the influence of the operating condition is concerned, we see that the scale d_{max} first increases from Cond 1 to 4, and then decreases from Cond 5 to 7. This evolution agrees with the observations in Fig. 5. We also note that the textural atomization processes involved structures whose scales range in a similar interval for all cases. The difference of $e_2(0)$ between the seven cases is not representative of the textural atomization process only. The characteristic $e_2(0)$ is the system specific length (defined as the perimeter per unit surface area, see Eq. (4)) and depends both on the system perimeter and surface area, the later one being not a textural atomization process characteristic. Therefore, the first task in the analysis will consist in splitting the scale distributions in Fig. 8 to isolate the component representative of the textural atomization process only.

Drop diameter distribution measurements and results

The drops produced from the textural atomization process in the near nozzle-exit region are measured by analyzing the images taken for this purpose (see the first part of this section). The image treatment involved steps similar to those exposed in Fig. 7 to produce segmented images with drops only appearing in black on a white background. The image model developed by Blaisot and Yon (2005) is applied in order to determine the contour of each droplet with the maximum possible accuracy. The image analysis reports an equivalent diameter for each drop as well as a shape parameter that quantifies its deviation from sphericity. The equivalent diameter is defined as $D = \sqrt{4S/\pi}$ where S is the drop projected surface area. For each condition, this analysis is performed on the 500 images ensuring a few thousands of drops for each measurement.

The surface-based scale distributions $f_2(D)$ of the drop diameters are built by considering spherical drops only recognized by their shape parameter. For ensembles of spheres, the surface-based distribution $f_2(D)$ is obtained from the number-based drop diameter distribution $f_0(D)$ with the relation:

$$f_2(D) = \frac{D^2}{D_{20}^{\,2}} f_0(D) \tag{10}$$

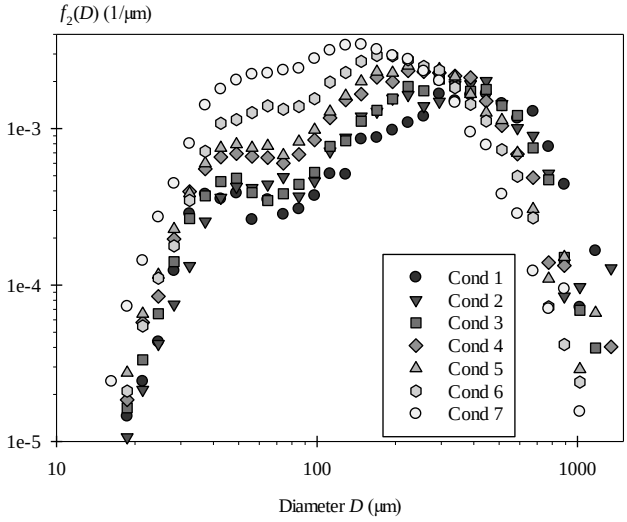

Fig. 9 Experimental surface-based drop diameter distributions

where D_{20}, for a set of spheres, is the surface mean diameter (Mugele and Evans 1951). The experimental drop diameter distributions $f_2(D)$ are plotted in Fig. 9.

Figure 9 shows that the drop diameter distributions of the textural sprays exhibit two modes. The right mode is the main one. It shows a peak diameter D_{peakR} that decreases when the flowrate increases. The peak diameter D_{peakL} of the left mode appears not affected by the mass flowrate but the drop population does: it increases with the flowrate. Considering that the textural atomization process consists of the rupture of ligaments, this kind of bimodal drop-diameter distribution could have been expected. Indeed, it is known that ligaments have a propensity to produce two drop categories, i.e., main droplets whose diameter is of the same order of the initial ligament size, and satellite droplets whose diameter is far less than the main-droplet one (Vassallo and Ashgriz 1991). The number and

size of the satellite drops depend on the initial shape of the ligament and on the physical mechanisms in play, and, more specifically, on the ratio between surface tension and elongation effects if any (Dumouchel et al. 2015).

4. Analysis

Mathematical scale-distribution of the textural atomization process

The first step of the analysis is to isolate the scale distribution of the textural atomizing structures from the measurements presented in Fig. 8. This is achieved with the help of the mathematical formulation established for the scale distribution in section 2 (Eq. (9)). This mathematical expression suits scale distributions with one single inflexion point whereas those measured in this work report two inflexion points (see Fig. 8). To reproduce this characteristic, the scale distribution is decomposed as the sum of two components:

$$e_2(d) = \beta_e e_{2,1}(d) + (1-\beta_e) e_{2,2}(d) \tag{11}$$

In this equation, $e_{2,1}(d)$ and $e_{2,2}(d)$ are two scale distributions represented by Eq. (9): they both depend on three parameters and they are both normalized. Since the experimental scale distribution is normalized also, the weighting parameter β_e ranges from 0 to 1. (This parameter actually represents the relative surface area of the ligament structures of the textural atomization process.) The application of Eq. (11) to fit the measured scale distributions requires the determination of seven parameters: (α_i, q_i, D_{q0i}) for each component and β_e. The fitting process is performed on the first derivative $e_2'(d)$ of the scale distributions. The calculation of these derivatives is completed by the condition $e_2'(0) = 0$ imposed for each case. For Cond 1 to 5, this condition reasonably agrees with the measurements but could not be verified for Cond 6 and 7 because of a lack of spatial resolution (limited to 37 µm) in the scale analysis. The scale distribution derivatives report two modes, each of them being associated with a derivative $e_{2,i}'(d)$: $e_{2,1}'(d)$ for the small scale mode, and $e_{2,2}'(d)$ for the large scale mode. Each mode is fitted with the derivative of Eq. (9) and the last parameter β_e is obtained from the surface area of each mode.

A Scilab routine was written to determine the set of parameters that provides the best fit of the measured scale distribution. The routine was applied for each condition, the solution for one condition being used as initial point to find the solution of the next condition. Although this routine reported results in most situations, the determination of the parameters α_1 and q_1 was proved difficult for Cond 6 and 7 for which a specific determination protocol has been followed. First, the parameter q_1 was evaluated from the correlation between the volume flow rate Q_v and the parameter q_1 obtained for Cond 2 to 5 (Regime I condition is not considered here). Second, the parameter α_1 is determined as the best fit provider conditioned by the constraint $e_2'(0) = 0$. For all conditions, this analysis returned very good fits of the experimental scale distributions.

In the decomposition described by Eq. (11), the component $e_{2,1}(d)$ is the scale distribution of the textural atomization process. The parameters of this component are listed in Table 2. The scale distributions $e_{2,1}(d)$ are calculated with Eq. (9) and plotted in Fig. 10. They spread to scales of the order of 1500 µm with a rather extended tail in the large-scale range. When the flowrate increases (from Cond 1 to 7), the scale distribution squeezes in the small scale range and its width decreases, but the distribution tails remain extended in the large scale range. These two behaviors combine in an increase of $e_{2,1}(0)$ when *CN* decreases and indicate that the ligament size-distribution shifts towards the small-size region, inducing an increase of the interface length per unit surface area.

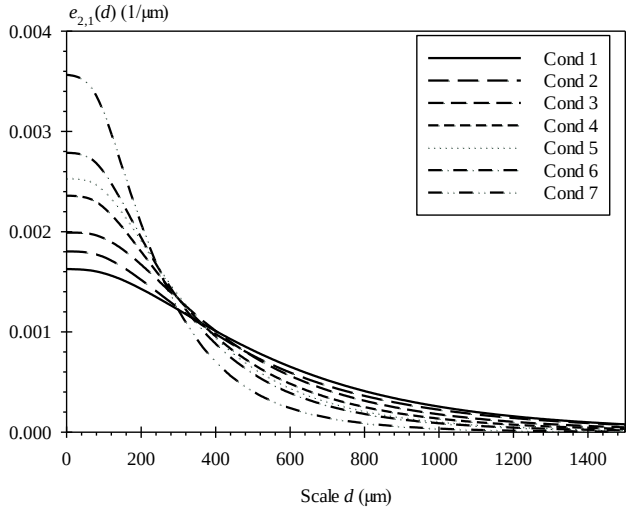

Fig. 10 Scale distributions of the textural atomization process

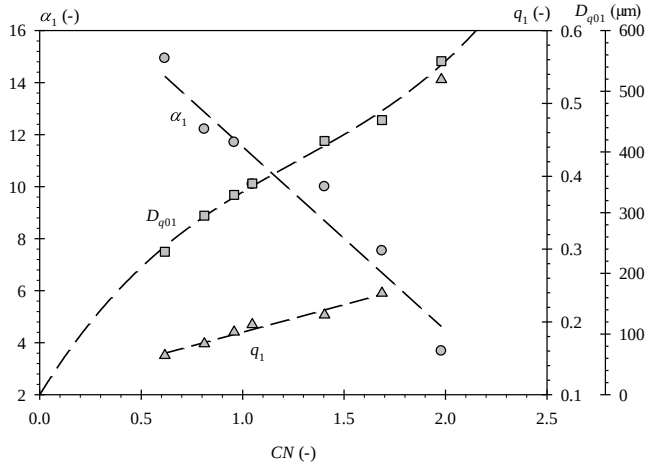

Fig. 11 Correlation between the parameter (α_1, q_1, D_{q01}) and the cavitation number *CN*

The three parameters of the distributions $e_{2,1}(d)$ correlate with the cavitation number *CN* (see Fig. 11) expressing the dependence between the flow regime and the textural atomization process. We first note that the values of D_{q01} are rather high considering the low order of this mean diameter (order being equal to the value of q_1). This, of course, is an illustration of the long tail in the large scale region noticed in Fig. 10. Therefore, being sensitive to the scale distribution tail, D_{q01} appears to be representative of the ligament size distribution, and its decrease with the cavitation number *CN* illustrates the production of finer and finer ligaments as the flow rate increases. Second, Fig. 11 shows that the dispersion parameters α_1 and q_1 show opposite variations. As explained in Section 2, the parameter q_1 is sensitive to the ligament size-distribution and the parameter α_1 to the distribution of scales associated with their deformation. The variations reported in Fig. 11 explain that, as *CN* decreases, the dispersion of the ligament size-distribution increases (q_1 decreases) whereas the dispersion of their deformation scales decreases (α_1 increases). This last behavior is associated with the decrease of the mean diameter D_{q01} illustrated in Fig. 11: the deformation-scale range shrinks because the ligaments are thinner.

Cond. N°	α_1 (-)	q_1 (-)	D_{q01} (µm)	d_p (µm)	$-e'_{2,1}(d_p)$ (µm^{-2})	d_{p2} (µm)	$-e''_2(d_{p2})$ (µm^{-3})
1	3.68	0.53	550	304	2.2 10^{-6}	70.5	1.35 10^{-8}
2	7.54	0.24	453	250	2.8 10^{-6}	71.8	2.22 10^{-8}
3	10.0	0.21	418	253	3.5 10^{-6}	85.8	2.68 10^{-8}
4	10.1	0.20	348	205	4.9 10^{-6}	66.6	4.67 10^{-8}
5	11.7	0.19	329	204	5.7 10^{-6}	72.4	5.44 10^{-8}
6	12.2	0.17	295	179	6.9 10^{-6}	61.6	7.60 10^{-8}
7	14.9	0.15	236	150	11.3 10^{-6}	56.5	14.7 10^{-8}

Table 2 Parameters of the textural atomization process scale distribution $e_{2,1}(d)$ and characteristic scales d_p and d_{p2}

The scale distributions of the textural atomization process in Fig. 10 all show one inflexion point, i.e., for one specific scale, called d_p: $e''_2(d_p)=0$. According to Eq. (7), we see that the scale d_p is also the modal diameter D_{p0} of the number-based diameter distribution of the cylinder equivalent-system. Therefore, in virtue of Eq. (3), it comes:

$$d_p = D_{q-1,-1} \tag{12}$$

The values of the scale d_p are given in Table 2 for all conditions. This scale is of the order of the half of D_{q01} and reports the same correlation with the cavitation number as this mean diameter. This specific scale is therefore representative of the size distribution of the ligaments involved in the textural atomization process. Another characteristic of the inflexion point is the derivative of the scale distribution at this scale, $e'_{2,1}(d_p)$ which is given by the following expression:

$$-e'_{2,1}(d_p)=\alpha_1\left(\frac{\alpha_1}{q_1}\right)^{\frac{1}{q_1}}\left(\frac{\alpha_1-1}{q_1}\right)^{\frac{(\alpha_1-1)}{q_1}}\frac{\exp\left(\frac{1-\alpha_1}{q_1}\right)}{{D_{q01}}^2} \tag{13}$$

Considering Eq. (7), $-e'_{2,1}(d_p)$ is proportional to the peak height of the cylinder equivalent-system number-based diameter distribution and, therefore, informs on the width of this peak. The values of $-e'_{2,1}(d_p)$ are given in Table 2. They were found to correlate with the cavitation number as

$-e'_{2,1}(d_p) \propto CN^{-1.35}$. This correlation indicates that, although the size distribution of the ligaments remains very much extended in the large scale region, the peak width of this distribution narrows on the diameter d_p when CN decreases. It appears therefore that the three parameters (q_1, d_p, $-e'_{2,1}(d_p)$) provide relevant properties of the ligament size-distribution including, its position in the size space (d_p), the dispersion around this peak ($-e'_{2,1}(d_p)$) and the dispersion in the upper size domain (q_1).

Mathematical diameter distribution of the spray drops

The second step of the analysis consists in deriving a mathematical expression for the surface-based diameter distribution $f_2(D)$ of the drops produced by the primary atomization process and shown in Fig. 9. The 3pGG distribution (Eq. (1)) is used for this purpose. As reported in Fig. 9, the experimental drop-diameter distributions show two peaks. Since the 3pGG distribution is a mono-modal function, a combination of two 3pGG distributions is required to fit the experimental results. The following decomposition is adopted:

$$f_2(D) = \beta_f f_{2L}(D) + (1-\beta_f) f_{2R}(D) \tag{14}$$

Seven parameters have to be determined: three for the left component $f_{2L}(D)$ characterizing the distribution in the small-diameter range (i.e., the satellite drops diameter-distribution), three for the right component $f_{2R}(D)$ characterizing the distribution in the large-diameter range (i.e., the main drops diameter-distribution), and the weighting parameter β_f. Two conditions are imposed in the parameter determination procedure. First, the two dispersion parameters that must have the same sign (Dumouchel 2006) are both taken positive for every component. Thus, the parameter α characterizes the dispersion in the small diameter space, whereas the parameter q controls the dispersion in the large-diameter range. Second, for each component, the experimental peak diameter (D_{peakL} or D_{peakR}) is imposed to the mathematical distribution. Using Eqs. (1-3), each component becomes:

$$f_{2*}(D) = \frac{q_*}{\Gamma\left(\frac{\alpha_*+2}{q_*}\right)} \left(\frac{\alpha_*+1}{q_*}\right)^{\frac{\alpha_*+2}{q_*}} \frac{D^{\alpha_*+1}}{D_{peak*}^{\alpha_*+2}} exp\left(-\frac{\alpha_*+1}{q_*}\left(\frac{D}{D_{peak*}}\right)^{q_*}\right) \qquad * = L \text{ or } R \tag{15}$$

The second condition reduces the number of parameters to be determined to 5. The determination of these parameters is performed with a Scilab routine written for this purpose. For every condition, the mathematical fit provided a very good representation of the measured drop-diameter distribution. The resulting parameters are listed in Table. 3. The values of the parameter β_f indicate the surface proportion represented by the left distribution peak $f_{2L}(D)$, i.e., by the satellite droplets. Table 3 shows that the evolutions of the dispersion parameters of the main drop population, i.e.,

α_R and q_R, are inverted. (These variations are similar to those reported by the parameters α_1 and q_1.) The width of the diameter distribution $f_{2R}(D)$ will be quantified by the ratio $\Delta_2 = (D_{42}^2 - D_{32}^2)/D_{32}^2$ (Δ_2 is the non-dimensional variance of $f_{2R}(D)$ introduced by Sowa (1992).) In virtue of Eq. (2), Δ_2 expresses as:

$$\Delta_2 = \frac{\Gamma\left(\frac{\alpha_R + 4}{q_R}\right)\Gamma\left(\frac{\alpha_R + 2}{q_R}\right)}{\Gamma^2\left(\frac{\alpha_R + 3}{q_R}\right)} - 1 \tag{16}$$

Cond. N°	D_{peakL} **(µm)**	D_{peakR} **(µm)**	α_L **(-)**	q_L **(-)**	α_R **(-)**	q_R **(-)**	β_f **(-)**
1	42	400	8.93	1.50	0.69	1.54	0.0077
2	48	335	9.67	1.66	0.79	1.37	0.0063
3	46	310	9.39	1.40	1.86	0.92	0.011
4	46	255	9.49	1.23	2.21	0.84	0.017
5	44	235	10.4	1.00	3.36	0.61	0.020
6	50	190	11.2	0.94	11.8	0.21	0.035
7	45	135	14.8	1.14	14.8	0.13	0.024

Table 3 Peak diameters of the drop diameter distribution and parameters of the mathematical fit

Correlation between the textural atomization process and the spray drops

The investigation of the correlation between the textural atomization process and the spray drops is conducted by relating the parameters attached to the atomization process to those representative of the spray. It is pertinent to remark at this stage that the scale distribution $e_{2,1}(d)$ and the diameter distribution $f_2(D)$ spread in the same scale interval. As mentioned above, the droplet diameter distribution shows two peaks. The correlation is established on the idea that the main-drop population (right peak of the distribution) is associated with the size distribution of the textural atomization ligaments, whereas the satellite population (left peak of the distribution) is associated with the deformation of these ligaments.

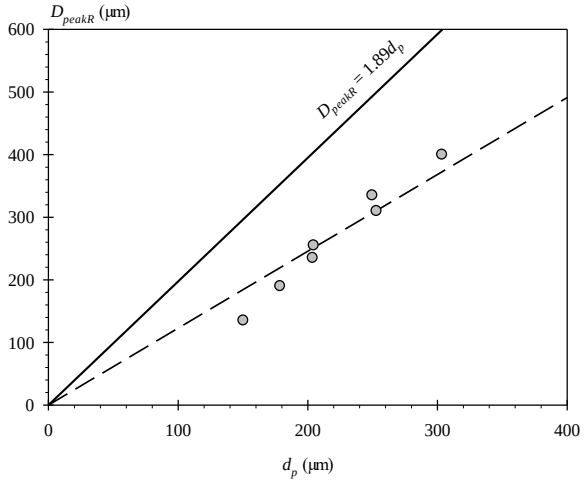

Fig. 12 Correlation between the scale d_p and the peak diameter D_{peakR}

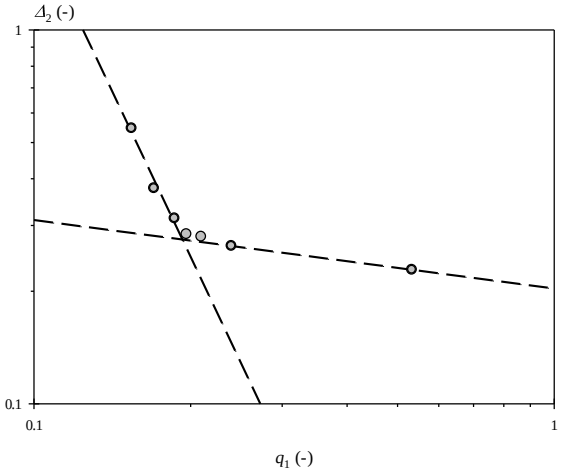

Fig. 13 Correlation between the parameter q_1 and the non-dimensional variance of the right peak of the drop diameter distribution (Eq. (16))

As far as the main drop population is concerned, the correlations obtained between the parameters (q_1, d_p, $-e'_{2,1}(d_p)$) and the parameters (α_R, q_R, D_{peakR}) validate the approach (Figs 12 to 14). First, Figure 12 shows that d_p and D_{peakR} are of the same order of magnitude:

$$D_{peakR} \approx 1.23 d_p \qquad (17)$$

This result confirms the fact that d_p is a characteristic size of the ligaments. The coefficient 1.23 is less than the theoretical coefficient 1.89 reported by Rayleigh (1878) for the breakup of a cylindrical smooth ligament due to capillary instability, probably because, being initially deformed, the ligaments are prompt to produce smaller drops as well as satellite droplets, the last point being attested by the measured drop diameter distributions (Fig. 8). These considerations and results evidence the major contribution of the surface tension effects, and, therefore, the negligible influence of the aerodynamic forces in the ligament breakup. Second, Fig. 13 reports a strong correlation between the dispersion parameter q_1 and the relative width of the main droplets diameter-distribution. As expected, an increase in the dispersion ligament size-distribution (q_1 decreases) induces an increase of the relative width of the main-drop diameter-distribution. Two tendencies, represented by the dash lines in Fig. 13, appear: as q_1 decreases, the first tendency corresponds to the flow Regimes I and II and the second one corresponds to the cavitation regimes III and IV. This observation could constitute a proof of a direct influence of the cavitation on textural atomization processes. Finally, Fig. 14 displays the correlation between the parameters α_R and $-e'_{2,1}(d_p)$. The positive derivative of this correlation says that the main-drop population disperses less in the small diameter range when the peak of the ligament size-distribution gets narrower.

The second peak of the drop-size distribution (left peak in Fig. 9) represents the satellite population. The number and size of these droplets depend on the deformation of the ligaments and should therefore correlate with the dispersion parameter α_1 of the atomization process scale distribution. It is important to mention here that the measurement of the left peak is less accurate than the one of the right peak. However, two interesting observations deserve to be presented.

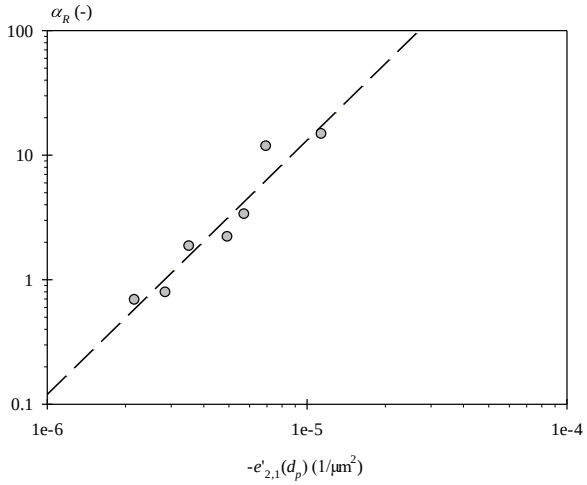

Fig. 14 Correlation between the parameter α_R and the derivative $-e'_2(d_p)$

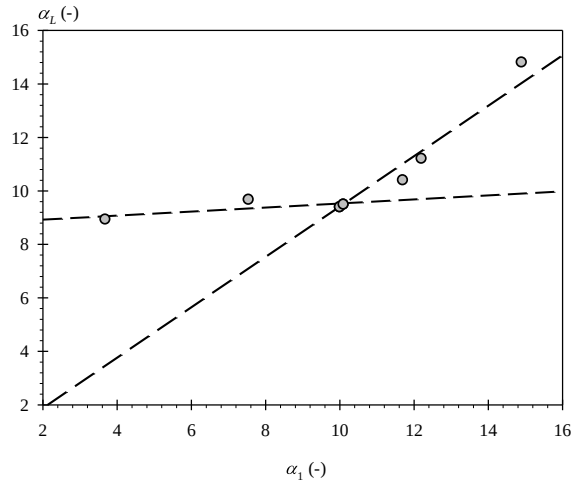

Fig. 15 Parameter α_L versus parameter α_1

First, taking inspiration from the previous analysis, we suggest introducing the first inflexion point of the function $-e'_{2,1}(d)$ (by *first* we mean the one obtained for the smallest scale). The scale at which this inflexion point is found is called d_{p2}.: $e'''_{2,1}(d_{p2}) = 0$. It appears that d_{p2} is almost constant such as the second diameter peak D_{peak2} (see Tables 2 and 3). Furthermore, $-e''_{2,1}(d_{p2})$ correlates with the cavitation number *CN* in a similar way as $-e'_{2,1}(d_p)$ ($-e''_{2,1}(d_{p2}) \propto CN^{-1.93}$). It correlates also with the parameter α_L again in a similar way as $-e'_{2,1}(d_p)$ with α_R (Fig. 14). (The parameter α_L characterizes the dispersion in the small-diameter range of the satellite droplets.) We understand that the successive inflexion points of a scale distribution and its derivatives identify representative scales as far as the drop diameter distribution is concerned.

The second observation concerns the correlation between α_1 and α_L (Fig. 15) which globally indicates that the dispersion in the small-diameter range of the satellite population increases with the one in the small-scale range of the ligament deformation. Two parts are identifiable in the figure: α_1 and α_L are of the same order of magnitude when $\alpha_1 > 10$, otherwise, the dispersion α_L appears rather constant (of the order of 10) whereas α_1 varies.

The cases $\alpha_1 > 10$ correspond to the high flow rates for which the textural atomizing ligaments are thin. This thinness imposes structural deformation and atomization only: the satellite droplet sizes

disperse in the diameter space in the same way as the small-deformation scales disperse in the scale space. This manifests by $\alpha_1 \approx \alpha_L$.

The cases $\alpha_1 < 10$ correspond to the low flow rate for which the textural atomizing ligaments are coarser and their deformation (characterized by α_1) is mainly textural but does not lead to the production of drops. Thus, the parameter α_L remains constant whereas the parameter α_1 still varies. This behavior reveals that, if the deformation scale is far less than the size of the ligament, it will not participate to the atomization process. This also explains that the amount of satellite droplets is less for these cases.

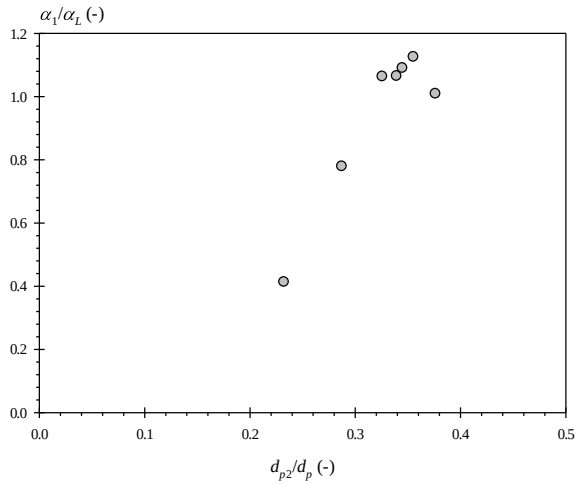

Fig. 16 Ratio α_1/α_L versus ratio d_{p2}/d_p

The result presented in Fig. 15 therefore indicates that the knowledge of the system deformation is not always necessary over the whole scale range, and this is the case if the ligament deformation scales are far smaller than the ligament deformation size. It occurs that the scale d_{p2} is a characteristic of the ligament deformation and the scale d_p is a characteristic of the ligament size. Therefore, the ratio d_{p2}/d_p should be appropriate to delimit the two behaviors found in Fig. 15. Figure 16 plots this ratio versus the ratio α_1/α_L. When $d_{p2}/d_p > 0.32$ (Cond 3 to 7) the satellite population depends on the ligaments deformation ($\alpha_1/\alpha_L \approx 1$). When $d_{p2}/d_p < 0.32$ (Cond 1 and 2), the satellite population is independent of the ligament deformation (α_L remains constant even if α_1 varies). In this second case, the resolution of the small ligament deformation is therefore not required. This result is another demonstration of the importance of the scales d_p and d_{p2}.

5. Conclusions

The multiscale method presented in this work appears to be very appropriate to experimentally investigate textural atomization processes such as those of this study and brings interesting results. The scale distribution it provides describes the atomizing ligamentary structures and includes information on the size distribution and on the deformation of these structures. To our knowledge, this is the only approach ensuring such a complete description. Furthermore, this multiscale method defines the concept of equivalent systems on which a mathematical representation of the atomization process scale distribution can be established. For the first time, an atomization process has received a mathematical expression. It is obtained from the mathematical diameter distribution of a set of cylinders that has the same scale distribution as the actual system. This approach is particularly adapted here since the atomization ligaments are rather cylindrical structures. The chosen mathematical distribution, i.e., the 3pGG function, was found very appropriate for this

purpose as well as to represent the spray drop size distribution. As far as the use of the 3pGG function is concerned, it is worth mentioning that three parameters are necessary to succeed in representing the scale distribution and the drop size distribution. They allow dissociating the drops produced by the larger ligaments from those produced by the more numerous. In the present study, these two populations evolved differently and required their own indicator (q or α) to be correctly taken into account.

The physical relevance of this mathematical expression has been evidenced by the correlations found between the three parameters it involves and the cavitation number of the flow on one hand, and the parameters of the diameter distribution of the drops on a second hand. These correlations allow deriving an atomization model where the spray main-drop population is related to the size distribution of the ligaments, whereas the spray satellite drop population is related to the ligament-deformation scale-distribution. This result demonstrates the possibility of evaluating the drop diameter-distribution from the textural atomization scale distribution. In this exercise, the scales at which the scale distribution and its derivative show an inflexion point are important. They inform on the typical size and dispersion in small diameter range of each drop diameter-distribution mode. Furthermore, their ratio indicates situation for which the deformation of the ligaments has no influence on the satellite drop production. Such information is practical and useful for modeling.

References

Arai M, Shimizu M, Hiroyasu H (1985) Break-up length and spray angle of high speed jets. 3rd International Conference on Liquid Atomization and Spray Systems, London, UK, 8-10 July 1985, paper IB/4

Babinsky E, Sojka PE (2002) Modeling drop-size distribution. Prog. Energy Combust. Sci., 28:303-328

Bérubé J, Jébrak M (1999) High precision boundary fractal analysis for shape characterization. Comput. Geosci. 25:1059–1071

Blaisot JB, Yon J (2005) Droplet size and morphology characterization for dense sprays by image processing: application to the Diesel spray. Esperiments in Fluids 39:977-994

Dumont N, Simonin O, Habchi C (2000) Cavitating Flow in Diesel Injectors and Atomization: A bibliographical review. 8th International Conference on Liquid Atomization and Spray Systems, Pasadena, CA USA, July 2000

Dumouchel C (2006) A new formulation of the Maximum Entropy Formalism to model liquid spray drop-size distribution. Part. Part. Syst. Charact. 23:468-479

Dumouchel C (2009) The Maximum Entropy Formalism and the prediction of liquid spray drop-size distribution (Review). Entropy 11:713-747

Dumouchel C (2017) Liquid Atomization and Spray: A multi-scale description. Proceedings of ASME-FEDSM, FEDSM2017-69590, July 30th, August 3rd, 2017, Waikoloa, Hawaii, USA

Dumouchel C, Blaisot JB, Bouche E, Ménard T, Vu TT (2015a) Multi-scale analysis of atomizing liquid ligaments, Int Journal of Multiphase Flow 73:251-263

Dumouchel C, Cousin J, Grout S (2008) Analysis of trwo-dimensional liquid spray images: The surface-based scale distribution. Journal of Flow Visualization & Image Processing 15:59-83

Dumouchel C, Ménard T, Aniszewski W (2015b) Towards an interpretation of the scale diffusivity in liquid atomization process: An experimental approach. Physica A 438:612-624

Fdida N, Blaisot JB (2010) Drop size distribution measured by imaging: determination of the measurement volume by the calibration of the point spread function. Meas. Sci. Technol. 21:025501 (15pp)

Fdida N, Mauriot Y, Ristori A, Vinger L, Chevalier PH, Théron M (2018) Primary Atomization of a Cryogenic LOX/N2 and LOX/He Jet in a Coaxial Rocket Injector. 14th Triennial International Conference on Liquid Atomization and Spray Systems, Chicago, IL, USA, July 22-26, 2018

Grout S, Dumouchel C, Cousin J, Nuglisch H (2007) Fractal Analysis of Atomizing Liquid Flows. International Journal of Multiphase Flows 33:1023-1044

He L, Ruiz F (1995) Effect of Cavitation on Flow and Turbulence in Plain Orifices for High-Speed Atomization. Atomization and Sprays 5:569-584

Kaye BH (1989) A Random Walk Through Fractal Dimensions. VCH, New York

Lecompte M, Dumouchel C (2008) On the Capability of the Generalized Gamma Function to Represent Spray Drop Size Distribution. Part. Part. Syst. Charact. 25:154-167

Lefebvre AH (1986) Atomization and Sprays. Hemisphere Publishing Corporation

Marmottant P, E. Villermaux E (2004) On spray formation. Journal of Fluid Mechanics 498:73-111

Rayleigh JWS (1878) On the instability of jets. Proceedings of the London Mathematical Society 10:4-13

Mugele RA, and Evans HD (1951) Droplet size distribution in sprays. Ind. Engng Chem. 43:1317-1324

Shavit U, Chigier N (1995) Fractal dimensions of liquid jet interface under break-up. Atomization and Sprays 5:525–543

Soille P (2004) Morphological Image Analysis. Springer-Verlag ISBN 978-3-642-07696-1

Soteriuo C, Andrews R, Smith (1995) Direct Injection Deisel Sprays and The Effect of Cavitation and hydraulic Flip on Atomization. SAE Technical Paper Series 950080, Detroit Michigan, February 27 – March 2, 1995

Sou A, Hosokawa S, Tomiyama A (2007) Effects of Cavitation in a Nozzle on Liquid Jet Atomization. International Journal of Heat and Mass Transfer 50:3575-3582

Sou A, Hendra Pratama R, Tomisaka T, Kibayashi Y (2012) Cavitation Flow in Nozzle of Liquid Injector. ICLASS 2012, 12th Triennial International Conference on Liquid Atomization and Spray Systems, Heidelberg, Germany, September 2-6:2012

Sowa WA (1992) Interpreting Mean Drop Diameters Using Distribution Moments. Atomization and Sprays 2:1-16

Tirel C (2019) Etude expérimentale de l'atomisation de structures ligamentaires viscoelastiques, PhD Thesis, Normandie Université, Université de Rouen , 2 avril 2019

Tirel C, Renoult MC, Dumouchel C, Lisiecki D, Crumeyrolle O, Mutabazi I (2017) Multi-scale analysis of a viscoelastic liquid jet. Journal of Non-Newtonian Fluid Mechanics 245:1–10

Vassallo P, Ashgriz N (1991) Satellite formation and merging in liquid jet breakup. Proc. R. Soc. Lond. 1 433:269-286

Villermaux E (2007) Fragmentation. Annu. Rev. Fluid Mech. 39:419-446

Villermaux E, Marmottant P, Duplat J (2004) Ligament-Mediated Spray Formation. PRL 92:074501

Vu TT, Dumouchel C (2018) Analysis of ligamentary atomization of highly perturbed liquid sheets. International Journal of Multiphase Flow 107:156-167

Wu PK, Miranda RF, Faeth GM (1995) Effects of initial flow conditions on primary breakup of nonturbulent and turbulent round liquid jets. Atomization and Sprays 5:175-196